



Conjugated asymmetry of the onset and magnitude of GPS scintillation driven by the vertical plasma drift

J. Sousasantos¹ · M. A. Abdu^{1,2} · E. R. de Paula² · A. O. Moraes³ · L. A. Salles¹ · B. J. Affonso¹

Received: 6 January 2021 / Accepted: 7 April 2022 / Published online: 9 May 2022
© The Author(s), under exclusive licence to Springer-Verlag GmbH Germany, part of Springer Nature 2022

Abstract

The equatorial plasma bubble evolution, its symmetric propagation away from the equator over north/south hemispheres, the vertical plasma drift asymmetry, and some implications between these phenomena are examples of the conjugate point experiment campaign results. However, the asymmetric transport of plasma may imply a distinct ionospheric background in each hemisphere. When the equatorial depletion reaches these regions, the ionospheric scintillation may present different patterns. In this work, data from scintillation monitors, ionosondes, and all-sky imagers deployed at geomagnetically antipodal stations around the equator during the campaign were evaluated along the months of October–December 2002. The results reveal asymmetries in the onset times and scintillation magnitudes. On the one hand, the scintillation onset occurred earlier in 80% of the cases over the southern hemisphere. On the other hand, 71% of the nights verified the larger scintillation values in the northern hemisphere. The distinct F region altitudes, thickness, bottomside electron density gradient scale lengths, and TEC over both stations seem to contribute to this asymmetric behavior.

Keywords Ionospheric scintillation · Scintillation onset · Scintillation latitudinal asymmetry · Scintillation spatial distribution

Introduction

The low-latitude nighttime ionosphere harbors diverse plasma phenomena. Its electrodynamical features are responsible for a variety of events among which the equatorial plasma bubbles (EPBs) and the ionospheric scintillation are prominent examples. These events are usually dependent on the solar flux, ionospheric conductivities, altitude of the ionospheric F layer, the vertical component of the plasma drift, seasonality, and bottomside density gradient scale length.

The EPBs are believed to be generated over the geomagnetic equator, at the F region bottomside, due to the so-called generalized Rayleigh–Taylor instability mechanism (Dungey

1956; Ossakow 1981; Haerendel 1973). These large structures of severe plasma depletion usually extend in tens to hundreds of kilometers in its zonal extension. During its vertical rise to progressively higher apexes, they stretch along the geomagnetic field lines extending to low-latitude conjugate regions in both directions of the magnetic flux tube (i.e., antipodal regions). Concurrent to its evolution, secondary instabilities develop in a cascading process, leading to the formation of steep gradients in progressively smaller scales (Haerendel 1973). Due to this turbulent development, there is an intrinsic relation between the EPB structures and ionospheric scintillation. The transionospheric signals suffer phase shifts and amplitude changes while crossing this irregular medium. The severity of the ionospheric scintillation is commonly evaluated using the amplitude scintillation index S_4 (Briggs and Parkin 1963; Whitney and Basu 1977; Yeh and Liu 1982; Kintner et al. 2007).

Several aspects of this phenomenology were studied. However, a complete understanding of its day-to-day variability and spatial distribution remains unaccomplished. For instance, the EPB events are now found to exhibit a conjugate point symmetry in its distribution along the geomagnetic field line (flux tube); notwithstanding, the background

✉ J. Sousasantos
jonasjs@ita.br

¹ Instituto Tecnológico de Aeronáutica (ITA),
São José dos Campos, Brazil

² Instituto Nacional de Pesquisas Espaciais (INPE),
São José dos Campos, Brazil

³ Instituto de Aeronáutica E Espaço (IAE),
São José dos Campos, Brazil

ionosphere in both hemispheres is often distinct. When intercepted by the EPBs originating from the equator, the diverse background in each hemisphere presumably implies different electron density gradients, which may cause changes in the scintillation behavior over each hemisphere. Recently, Zhao et al. (2021) using 36 Global Network Satellite System (GNSS) receivers around the globe found larger rates of irregularities over southern hemisphere along the American sector. They used the rate of change of total electron content (TEC) over 5 min, referred to as ROTI, along the nights. Their results illustrate that some asymmetry seems to be present. Previously, Luo et al. (2019) used data from Swarm-A and Swarm-C satellites and information from two ground-based geomagnetically conjugate Global Positioning System (GPS) stations along the African sector to investigate the behavior of the plasma irregularities and scintillation. Their analysis considered the electron densities along Swarm satellites orbit altitudes (450 km), the ROTI, and the amplitude scintillation for the period evaluated. The results presented by the authors suggest a transition of scintillation onset times between northern and southern conjugate stations across September–December 2015 and March 2016, and the authors argued that the sunset time was a potential candidate to explain such asymmetries, although their results under decreased solar activity were slightly different. These findings suggest the existence of possible mechanisms behind asymmetric behavior over conjugate points; therefore, further investigations are required to uncover the mechanisms that, for a given EPB structure, may lead to distinct scintillation patterns. Over the Brazilian region, due to idiosyncrasies such as large geomagnetic declination and steep geomagnetic strength decrease, the scenario is distinct from that of Africa, and the investigation may offer new insights about the asymmetric patterns of the ionospheric scintillation. Along with this work, data from the Conjugate Point Equatorial EXperiment (COPEX) campaign (Abdu et al. 2009) in the Brazilian territory during the year of 2002 (maximum solar cycle period) will be explored to study new aspects of the spatiotemporal distribution of the scintillation.

Stations and instruments used in this work

The Conjugate Point Equatorial EXperiment (COPEX) was carried out during the months of October–December in 2002. Several instruments were deployed at three locations: an equatorial station, Cachimbo (CB), the northern conjugate station Boa Vista (BV), and the southern conjugate station Campo Grande (CG). A schematic of the instrument locations is presented in Fig. 1. The red curve corresponds to the dip equator. The black arc represents a given geomagnetic field line whose apex passes over Cachimbo (CB), and the field line northern/southern “feet” are over Boa Vista

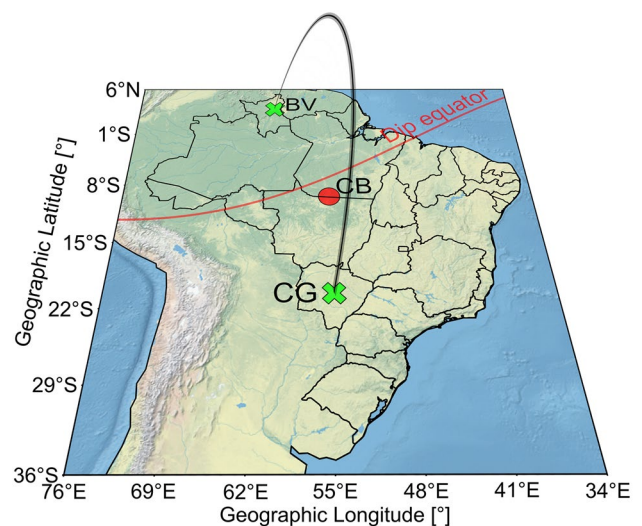


Fig. 1 Schematic of the COPEX geometry depicting the sites of the equatorial station Cachimbo (CB) in red, and the northern/southern conjugate stations Boa Vista (BV)/Campo Grande (CG), both in green color. The red curve represents the dip equator, and the black arc corresponds to a given geomagnetic field line connecting the stations

(BV)/Campo Grande (CG). The description of coordinates and instruments used in each location (in this work) is summarized in Table 1.

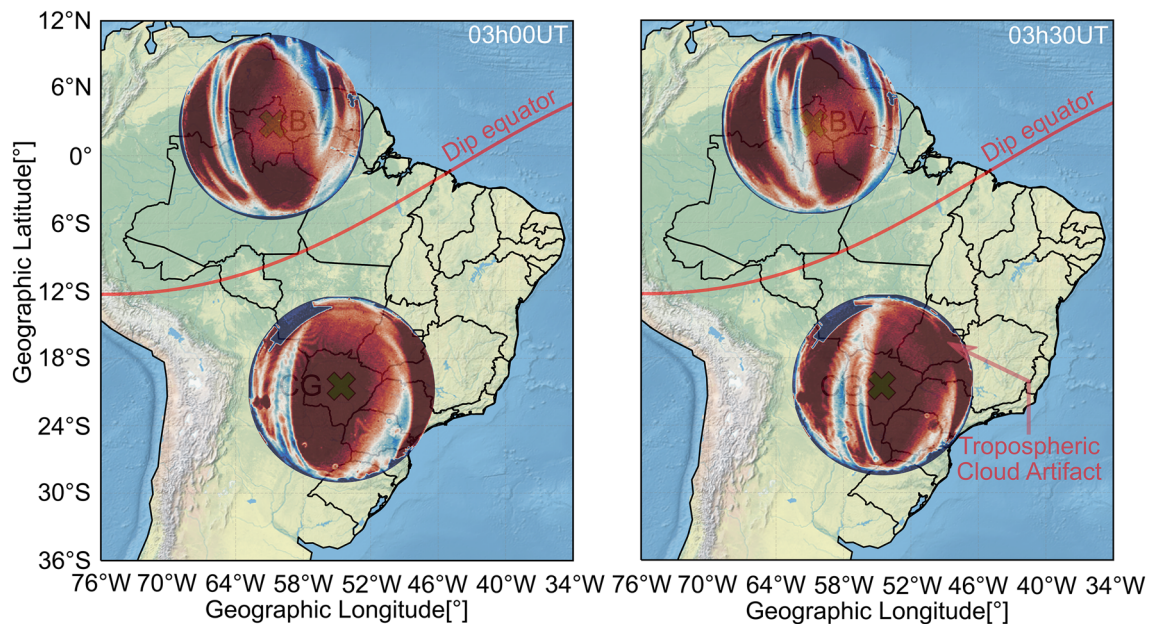
Digisonde data were used to calculate the true vertical drift, especially around the evening Pre-Reversal Enhancement in the zonal electric field (PRE). The PRE is largely responsible for the development of the EPBs and the scintillation (Abdu et al. 2009 and references therein, Sousasantos et al. 2013, 2018, 2019, Huang 2018, Resende et al. 2019). The calculation considers the temporal rate of change in the F layer true heights, $d(hF)/dt$, at the plasma frequencies 4 MHz, 5 MHz, 6 MHz, and 7 MHz. All-sky images were used only to exemplify the EPB mapping as discussed in Abdu et al. (2009) (Fig. 3 in their paper) and Sobral et al. (2009) (Fig. 2 in their paper). Data from scintillation monitors were used to evaluate the day-to-day onset of the scintillation in the Global Positioning System (GPS) L1 signals, the amplitude scintillation index (S_4), and the magnitude of the scintillation events on each night.

Equatorial plasma bubble over conjugate points and related scintillation patterns

It is now well understood that the EPBs begin their development at the equatorial F layer bottomside, and with its vertical rise over the equator, their extremities extend along the geomagnetic field lines to both (northern/southern) hemispheres. However, in the case of ionospheric scintillation,

Table 1 Coordinates and instruments deployed at each of the stations used in this work

Station	Geographic longitude (°)	Geographic latitude (°)	Magnetic latitude (°)	Instruments (in this work)
Cachimbo (CB)	54.8°W	9.8°S	2°S	Digisonde
Boa Vista (BV)	60.7°W	2.8°N	11°N	All-sky imager Scintillation monitor Digisonde
Campo Grande (CG)	54.7°W	20.5°S	11°S	All-sky imager Scintillation monitor Digisonde

**Fig. 2** EPBs registered by the all-sky imagers at stations BV and CG during the night of Oct. 9, 2002. The red/blue colors correspond to larger/lesser electron density concentration. Airglow depletion images reveal similar EPB events over both conjugate stations

the role of the background ionosphere is of great significance. Moraes et al. (2018a, b, c) showed that the scintillation is stronger over regions with more background plasma density; hence, the scintillation during the post-sunset and pre-midnight hours becomes more intense at locations approaching the crests of the Equatorial Ionization Anomaly (EIA). Although there is a close relationship between the EPBs and scintillation, stronger scintillation events are usually verified over low latitudes instead of the magnetic equator, where the EPBs were generated. This fact suggests that under distinct conditions of the background ionosphere, the scintillation events arising as a result of the same (mapped) EPB event may present slightly dissimilar patterns.

Figure 2 exhibits all-sky airglow depletion images (OI 6300 Å) for the conjugate stations BV and CG on the night of Oct. 9, 2002 at 03h00 and 03h30 UT. The red/blue colors indicate larger/lesser emission intensity (plasma density). It may be noticed that both stations observed

very similar EPB events (elongated blue streaks), but the airglow intensity (darker red regions) seems to be slightly different over each hemisphere. Plasma background differences may be attributed, in general, to distinct meridional wind components or geomagnetic field configuration and ensuing plasma drift components. However, in the present case, the southern hemisphere EPB structure (at east) in the right panel was partially covered by tropospheric cloud artifacts. The plasma depletions (north–south elongated streaks) seem to be slightly darker in the northern hemisphere, perhaps indicating distinct background and larger plasma density gradients (background/depleted EPB) for these particular frames.

In order to assess the scintillation occurrence during these EPB events, the amplitude scintillation index (S_4) was calculated from monitors deployed at stations BV and CG. The S_4 index is computed as the standard deviation of the normalized signal power over 60 s, namely:

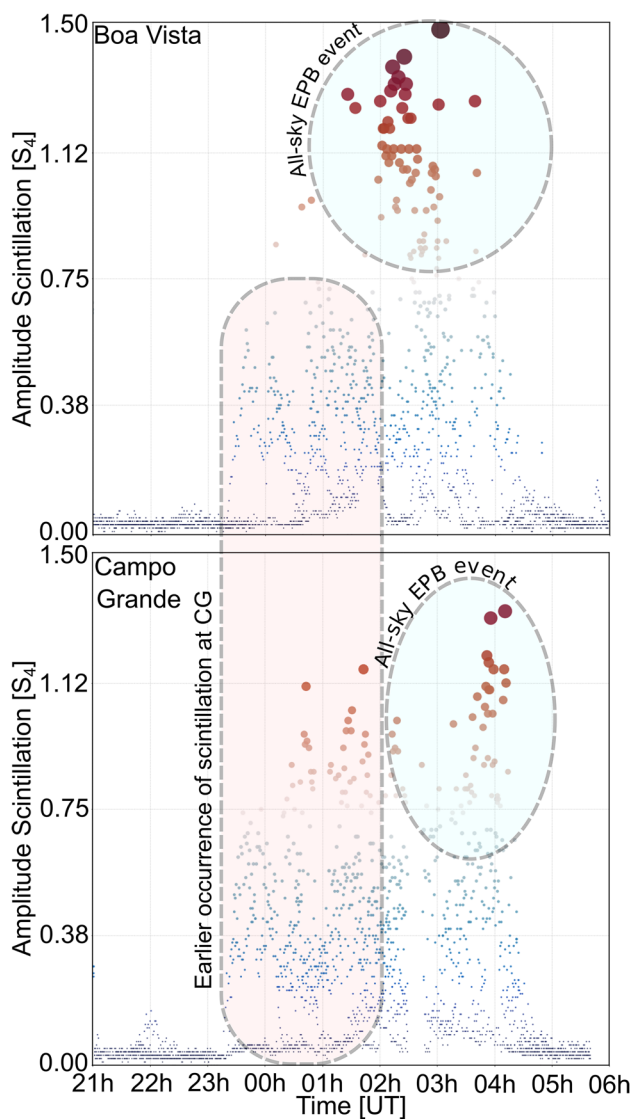


Fig. 3 Temporal evolution of the amplitude scintillation (S_4) for BV (upper panel), and CG (lower panel) on the night of Oct. 9, 2002. Blue/red dots indicate weaker/stronger amplitude scintillation. The cyan/red highlighted areas denote those all-sky EPB frames/earlier occurrence of scintillation over station CG, respectively

$$S_4 = \sqrt{\frac{\langle I^2 \rangle - \langle I \rangle^2}{\langle I \rangle^2}} \quad (1)$$

with $I = A^2$, where I = signal intensity, A = amplitude of the signal, and $\langle \rangle$ denotes the temporal average. The scintillation monitors used in this work were the Cornell scintillation monitors (CSM). These monitors acquire up to 11 GPS satellites simultaneously with one channel devoted to noise floor estimation. The sample rate for each channel is 50 Hz (Beach and Kintner 2001). An elevation angle mask was applied to exclude any data registered at angles $< 30^\circ$ in order to avoid multipath signals and very long path length

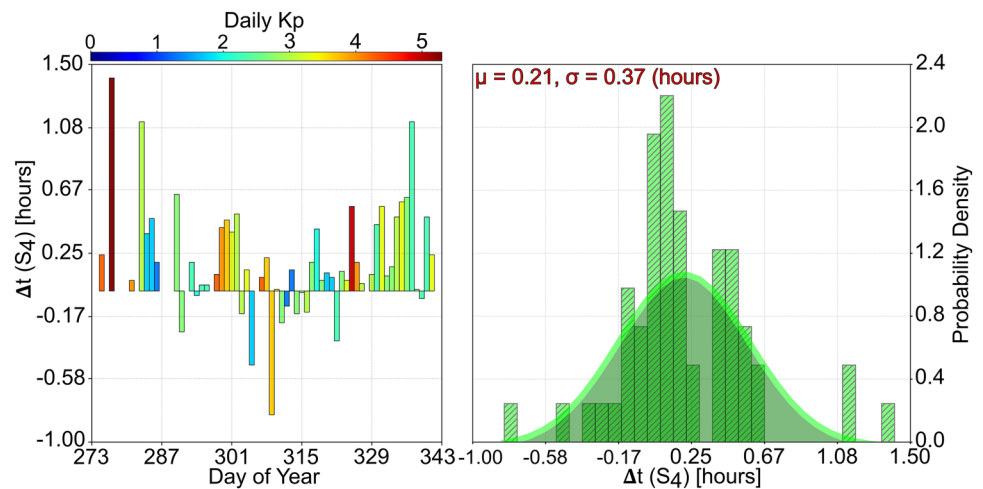
where scintillation over other locations could be merged with the dataset of interest. Over the entire dataset, at least 5 satellites were always tracking the scintillation with this elevation angle requirement. The analyses presented in the next sections consider all these measurements instead of individual satellite records. One example of the results of the S_4 is presented in Fig. 3, where the temporal evolution of the scintillation during one night (Oct. 9, 2002) is depicted for BV (upper panel) and CG (lower panel). The blue/red dots indicate weaker/stronger scintillation. The sizes of the dots are related to its magnitude. Please notice that since the all-sky coverage is wide (1100 km) and the EPB zonal drift over Brazilian region during these hours is typically < 100 m/s (Sobral et al. 2009), it is reasonable to assume that the areas highlighted in cyan correspond to those all-sky EPB frames shown in Fig. 2. Clearly, the EPBs exhibited in Fig. 2 are present here in the form of amplitude scintillation (contained in the cyan areas); notwithstanding, some details found in Fig. 3 deserve special attention. Although both stations undergo the same EPB event, the scintillation peaks and onsets are not the same. The scintillation contained in the red shaded area indicates a slightly earlier concentration of strong S_4 events over station CG. Also, it is possible to notice that the amplitude scintillation reaches larger values over the BV than CG. Hence, the scintillation pattern may present some deviations over conjugate points experiencing the same mapped EPB structures. Please notice that earlier onset may be verified even for values as low as $S_4 = 0.2$, and in the case of this illustrative example, the onsets difference is about 8 min.

GPS scintillation onset and magnitude over conjugate points

Following the results from Fig. 3, an investigation of the scintillation pattern over stations BV and CG was performed using the available dataset that covers October 5 to December 10, 2002. However, due to some lack of data, or outliers in the dataset in one of the stations, a total number of 55 nights were available for comparison in the present work. As aforementioned, an elevation angle mask was applied to remove registers with elevation $< 30^\circ$. Furthermore, only $S_4 > 0.2$ were considered, and in this work, its first occurrence is assumed as scintillation onset. The dataset was evaluated day-by-day and station-by-station, manually in order to avoid any false positive. When concomitant events were found, that recorded with the largest elevation angle was selected to represent the result for that specific moment.

The first analysis regards the difference in the scintillation onset time over stations BV and CG, and the results are exhibited in the form of bars in the left panel of Fig. 4. The onset time difference between the stations, Δt , was

Fig. 4 Distribution of Δt (S_4) and its statistical behavior. Left panel: Time difference of scintillation onset over BV and CG during COPEX campaign. The cold/hot colors in each bar indicate lesser/larger geomagnetic activity on the day when scintillation was observed. Here $\Delta t = BV(t) - CG(t)$. Right panel: distribution of the Δt values revealing a mean value (μ) of 0.21 h (about 12 min) with standard deviation (σ) equivalent to 0.37 h (about 22 min)



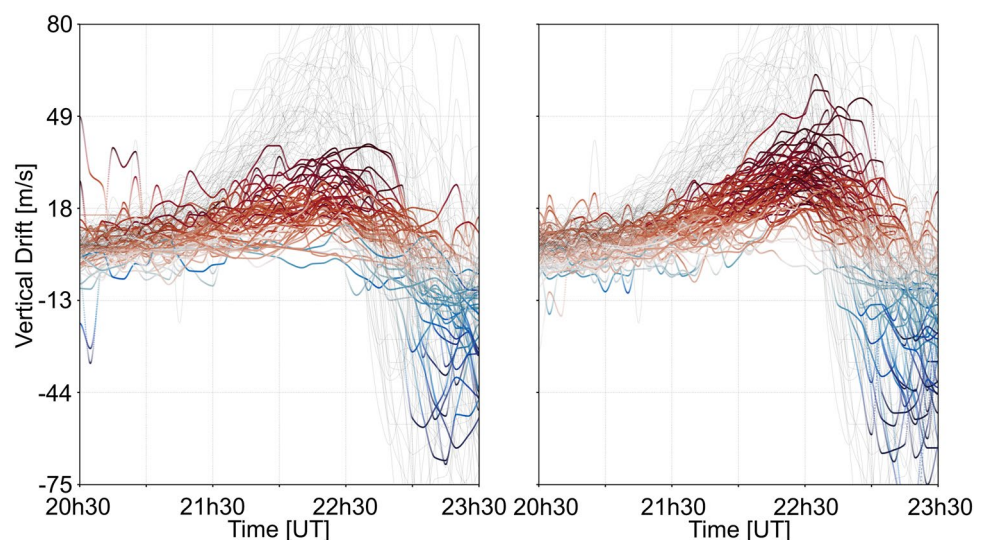
calculated considering the time of occurrence in UT, following $BV(t) - CG(t)$, i.e., positive/negative values correspond to earlier onset over CG/BV. Here, the notation follows the format station(*parameter*), and t is the time of scintillation onset. The colder/hotter colors of each bar are related to lesser/larger geomagnetic activity, measured by the daily K_p largest value.

According to the left panel results, most days show later S_4 onset over BV (i.e., $\Delta t > 0$). In fact, 80% of the cases (44 cases) presented $\Delta t > 0$. This difference in the onset time is usually of the order of a few tens of minutes; however, it may exceed 1 h in exceptional cases.

The right panel of Fig. 4 exhibits the distribution of the Δt values. The mean value (μ) of these differences in the S_4 onset (Δt) is 0.21 h (about 12 min), with a standard deviation (σ) of 0.37 h (about 22 min). It must be noted that the geomagnetic activity was calm during most of the analysis period and did not play any substantial role in the trend found in the dataset.

One of the most relevant aspects revealed during the COPEX campaign concerns the asymmetry in the vertical component of plasma drift over conjugate points (Abdu et al. 2009; Sousasantos et al. 2020). Using Digisonde data, the authors demonstrated that the vertical plasma drift over BV and CG presented different magnitudes, mainly during the evening pre-reversal vertical drift. The vertical drift over station CG (southern hemisphere) is often larger than that over station BV (northern hemisphere). In both works, the authors verified that an average northward transequatorial wind was potentially causing the asymmetry. Figure 5 shows the vertical plasma drifts during the COPEX campaign over BV (left panel) and CG (right panel) plotted in colored lines (blue/red indicating lesser/larger values). The gray lines correspond to the vertical drifts over the equatorial station CB for the same days and are provided as a reference. Based on the asymmetric vertical drift behavior presented in Fig. 5, one must expect that the ionospheric background at each hemisphere may present considerable differences in terms

Fig. 5 Plasma vertical drift over BV (left panel) and CG (right panel) during COPEX campaign (October 1 to December 31, 2002) represented by colored curves (blue/red indicating lesser/larger values). The gray lines correspond to the vertical drifts over Cachimbo equatorial station and are given as a reference



of bottomside altitude, electron density gradients, etc. This may account for the Δt verified in the scintillation onset.

Another aspect of interest was investigated by Sobral et al. (2009). The authors evaluated the zonal component of the plasma drift during the COPEX campaign using images registered through all-sky imagers deployed at BV and CG. They found slightly larger values of the velocity over CG (southern station) in their work. The difference was attributed to the geomagnetic anomaly over the southern Brazilian territory. In fact, during the period of the COPEX campaign, the geomagnetic field intensity (i.e., F component) over BV was about 25,321 nT, and over CG, closer to the South Atlantic Magnetic Anomaly (SAMA), the value was about 20,057 nT. Both plasma drift components over the stations are inversely proportional to the geomagnetic field (i.e., $V \propto E/B$). If the zonal component increased due to a decreased B , an enhancement is also expected in V_z .

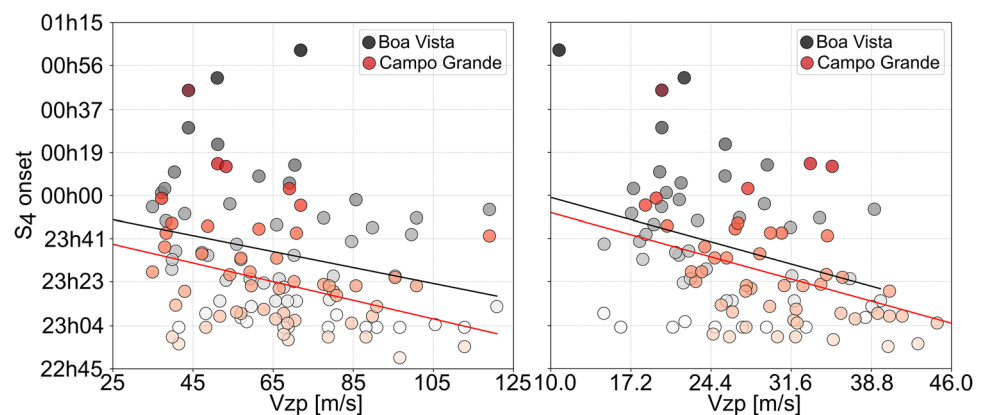
Using data from zonally spaced GPS (1575 GHz) and VHF (250 MHz) receivers during the COPEX campaign, de Paula et al. (2010) found that hundred-meter scale structures causing L-band scintillations appear to be drifting (zonal component) with equivalent velocities over both conjugate stations. However, the zonal drift of the kilometer-scale structures over CG presented slightly larger average velocities at times up to 03h00 UT. The authors used an argument similar to Sobral et al. (2009) to justify these results. Therefore, the works of Abdu et al. (2009), Sobral et al. (2009), de Paula et al. (2010), and Sousasantos et al. (2020), indicate that at least two agents may cause distinct plasma drift components between the hemispheres, the meridional (transequatorial) winds, and the geomagnetic field idiosyncrasies. These differences in the plasma drifts may alter the whole ensuing situation and are strong candidates to explain the differences verified in Fig. 4.

It is well known that EPB events, and the associated ionospheric scintillation, are closely related to the vertical drift magnitude (Fejer et al. 1999). Abdu et al. (2009) verified that the peak value during the PRE (V_{zp}) must attain 22 m/s over the equator for the spread F development. However, it is

worth noting that the vertical drift pattern over the equator and conjugate points may bring in, indirectly, other consequences. Figure 6 shows a day-by-day comparison between the S_4 onset time (in UT) in both conjugate stations (BV and CG) and the PRE vertical drift peak (V_{zp}). The left panel shows a plot of the S_4 data over BV (gray circles) and over CG (red circles) versus the values of V_{zp} over the equatorial station (apex) of CB. The right panel shows a similar comparison, however; this time, the S_4 data of each station are juxtaposed with the V_{zp} value over the same station instead of that over the equator, i.e., $BV(S_4) \times BV(V_{zp})$ and $CG(S_4) \times CG(V_{zp})$. The black/red lines correspond to linear regressions of data from BV/CG. The results presented in the left panel show that S_4 occurrences are typically verified for equatorial values of $V_{zp} > 20$ m/s. Moreover, the linear regressions in both panels reveal a decrease in the onset time with the increase in the V_{zp} values, as expected. Notwithstanding, it must be noticed that the S_4 onset over station CG is predominantly earlier than that over station BV. This behavior is independent of the V_{zp} values in both approaches, either considering the equatorial V_{zp} values (left panel) or considering $BV(S_4) \times BV(V_{zp})$ and $CG(S_4) \times CG(V_{zp})$, as shown in the right panel. However, the right panel exhibits more similar slope trends when each station is compared with its own V_{zp} , suggesting the major role of the local background in the result. In fact, the vertical drift over station CG is consistently higher than that over BV (Abdu et al. 2009, or Fig. 5), independent of the equatorial V_{zp} value.

Another aspect evaluated in both conjugate stations was the maximum daily value of the amplitude scintillation. A day-by-day subtraction of the maximum values [$\Delta S_4 = BV(\max|S_4|) - CG(\max|S_4|)$] was performed and the results are presented in the left panel of Fig. 7. The maximum S_4 values over each station occurred, sometimes, at slightly different times; however, the results presented in the left panel intend to show the largest value during the night and consider the peak values over each station, regardless of its time UT. The dashed gray line indicates the equivalence

Fig. 6 S_4 onset according to the V_{zp} values. Left panel: comparison between S_4 onset over the BV (gray circles) and CG (red circles) stations and the V_{zp} values over the equator. Right panel: comparison between S_4 onset and the V_{zp} values over each station, i.e., $BV(S_4) \times BV(V_{zp})$ and $CG(S_4) \times CG(V_{zp})$. The black/red lines correspond to linear regressions of data from BV/CG



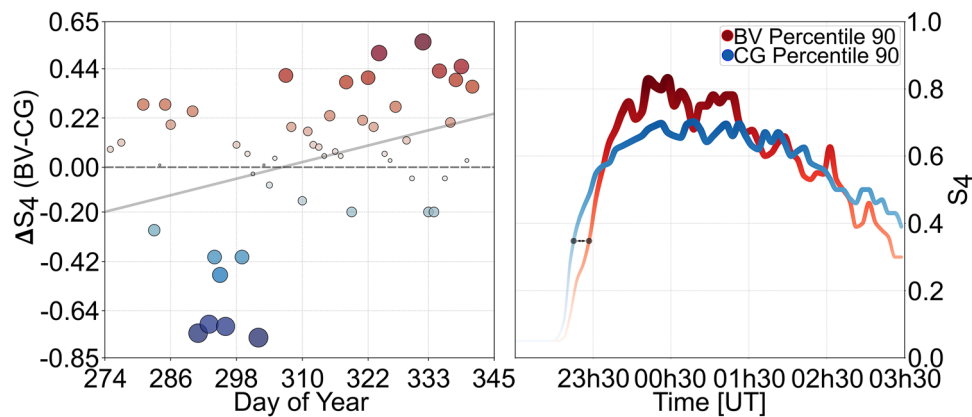


Fig. 7 Scintillation peak differences (ΔS_4) and the percentiles 90 over the conjugate stations. Left panel: difference of maximum amplitude scintillation over stations BV and CG. The dashed gray line represents $\Delta S_4=0$, and the solid line corresponds to a linear regression of

level, $\Delta S_4=0$, the solid gray line represents a linear regression of the dataset, and the cold to hot colors/size of the dots correspond to increasing values of ΔS_4 . Please notice that the regression line was inserted only to indicate (qualitatively) a seasonal transition. According to these results, the amplitude scintillation is more pronounced over station BV in 71% of the cases (39 days), with 16 of these 39 days reaching $\Delta S_4 \geq 0.2$. Only in 29% of the cases, the scintillation is stronger over CG (i.e., $\Delta S_4 < 0$), and the number of days when $\Delta S_4 \leq -0.2$ is 8. The solid gray line highlights that this trend of higher values of S_4 over BV station seems to increase toward summer solstice (in the southern hemisphere), when vertical drift is maximized over the Brazilian region. Hence, according to the dataset, the S_4 onset is often verified earlier over station CG, whereas the larger values are registered usually over station BV, thus suggesting asymmetries in time and magnitude of scintillation over the conjugate stations experiencing the EPB events.

The right panel of Fig. 7 exhibits the percentile 90 of all available datasets for both stations. Each percentile considers bins of 5 min of time to gather a representative amount of records. The resolution of S_4 measurements is 60 s; therefore, for one given satellite available, at least 275 measurements were considered. Since the receivers recorded data from 11 satellites, this number may reach 3025 records per bin. The red/blue curves correspond to the results for stations BV and CG. The results clearly show that most of the largest values over CG were smaller than those in BV. This is in good agreement with the left panel and indicates that this is a consistent trend. Also, the occurrence of $\Delta S_4 > 0$ seems to be concentrated in the early nighttime period, $23\text{h}30 \text{ UT} \leq t \leq 01\text{h}30 \text{ UT}$ (i.e., $19\text{h}27 \text{ LT} \leq t \leq 21\text{h}27 \text{ LT}$ for station BV). Additionally, the right panel of Fig. 7 again demonstrates that the earlier S_4 onset over station CG (blue

curve) is a predominant trend. The black dots and the arrow between the curves for CG and BV denote the time interval when S_4 attains values larger than 0.2. The difference between the onsets at these points reaches $\Delta t = 11.87$ min, very close to the average value of $\mu = 12$ min presented in the discussion of Fig. 4; therefore, both asymmetries regarding S_4 onset and peak values seem to occur coherently over the entire dataset.

Discussion

Abdu et al. (2020) showed that under distinct bottomside electron density gradient scale lengths, the development of the EPB structures is different. Their results suggest that in cases where V_{zp} is large, the EPB structures usually present larger velocities, hence reaching higher altitudes and vice versa. Moreover, they also found that under smaller V_{zp} conditions, usually, a steeper electron density vertical gradient is verified. This can be understood in terms of a larger loss rate through chemical recombination in this lower ionosphere bottomside in the case of smaller V_{zp} . Furthermore, in the case of smaller V_{zp} , they also found that the vertical instability growth is reduced, and the spread F growth usually cannot cross the bottomside region, but the degree of depletion in these bottomside altitudes is typically stronger. Additionally, their findings indicate that under stronger V_{zp} conditions, the rise of the F layer height is normally accompanied by a vertical extension of the layer, increasing the thickness of the F region, consequently decreasing the bottomside electron density (vertical) gradient scale length (L^{-1}). The electron density vertical gradient scale length is given by:

$$L^{-1} = \left(\frac{1}{N_e} \right) \left(\frac{\partial N_e}{\partial h} \right) \tag{2}$$

where N_e is the electron density and h the altitude (true height).

The discussion presented in Abdu et al. (2020) deals strictly with differences verified between solar maximum and minimum conditions; however, let the implications of their findings be used from another perspective; namely, distinct Vz_p patterns implied dissimilar F region configurations. In this case, this component may be added to the discussion of scintillation asymmetries between stations.

Figure 8 shows one example of the slope of the F region bottomsides over BV (upper left panel) and CG (lower left panel) for the same night. The red and cyan (magenta and purple) solid lines in the ionograms in these panels depict the slope of the F region over BV and CG, respectively. These panels show that, in terms of slope, the values over BV are larger for smaller and larger frequencies/densities (i.e., lower and higher bottomsides altitudes). Please notice that the frequency/ N_e varies more pronouncedly over BV than over CG for a smaller altitudinal range.

The upper right panel exhibits the electron density vertical profiles and the bottomsides gradient scale length for stations BV and CG in a frame prior to a spread F event on this arbitrary night (November 26, 2002). The blue/red colors along the curves correspond to lesser/larger calculated values of the bottomsides electron density gradient scale length

(L^{-1}), detailed in the color bar. This panel shows that the thickness of the F region is broader over station CG, and its F region peak (hmF2) is higher than over station BV. The hmF2 values over CG/BV were 552/454 km. Consequently, the bottomsides gradient scale length over station BV is larger. These features comply with the differences in the Vz_p patterns [BV(Vz_p)=22 m/s and CG(Vz_p)=63 m/s] and the implications on the background configuration analogously to the discussed in Abdu et al. (2020).

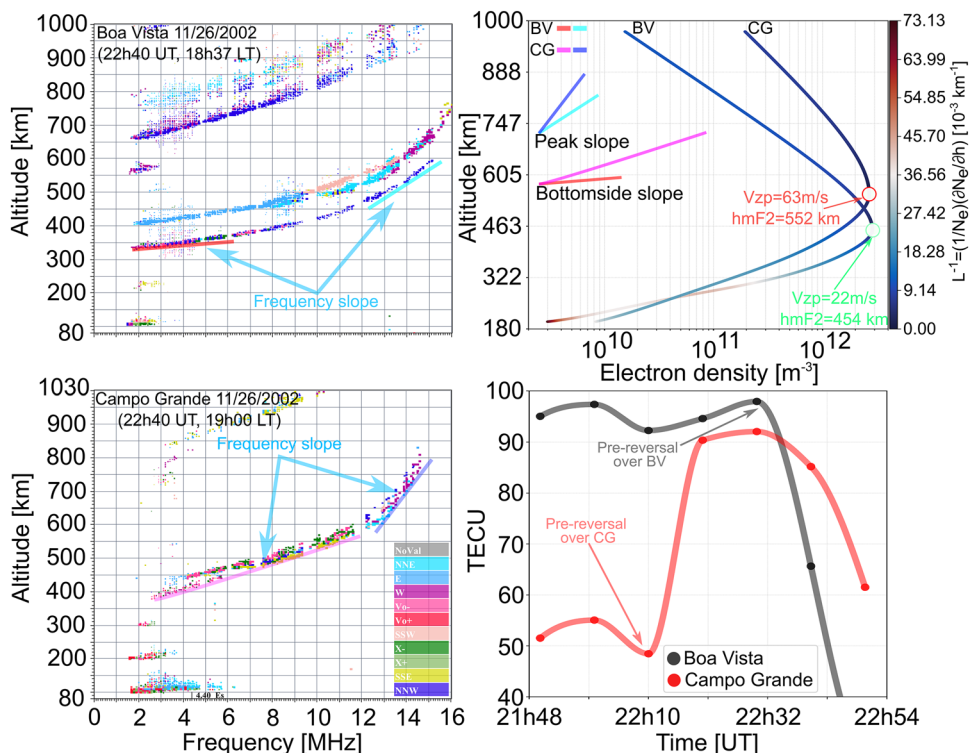
The lower right panel shows the results of numerical integrations of the vertical electron density profiles (transformed into total electron content, TEC, units) for several frames around the PRE for BV/CG (black/red) on the night of November 26, 2002. The numerical integration was performed according to the simplified central scheme:

$$\left(\frac{10^{-16}}{2} \right) \sum_{i=1}^{n-1} N_e(i) [h_{(i+1)} - h_{(i-1)}] \tag{3}$$

where h is the altitude (true height) and n is the number of discrete vertical points.

The results presented in the lower right panel indicate that the total electron content (TEC) difference between BV and CG varies in the range $-19 < \Delta \text{TEC} < 43$ (TECU). The value of 1 TECU = 10^{16} electrons/m². It must be noticed that the initial values over station CG were considerably lesser than those over BV. However, when station CG undergoes the PRE effects, the TEC is suddenly increased, suggesting

Fig. 8 Ionograms showing the F region slope over BV (upper left panel) and CG (lower left panel). The red and blue (magenta and purple) solid lines highlight the slope trend over BV (CG). Upper right panel: N_e vertical profiles and bottomsides electron density gradient scale lengths (L^{-1}) over BV and CG. Lower right panel: integrated vertical N_e along several frames around the PRE for the stations of BV and CG on the night of November 26, 2002 (11/26/2002)



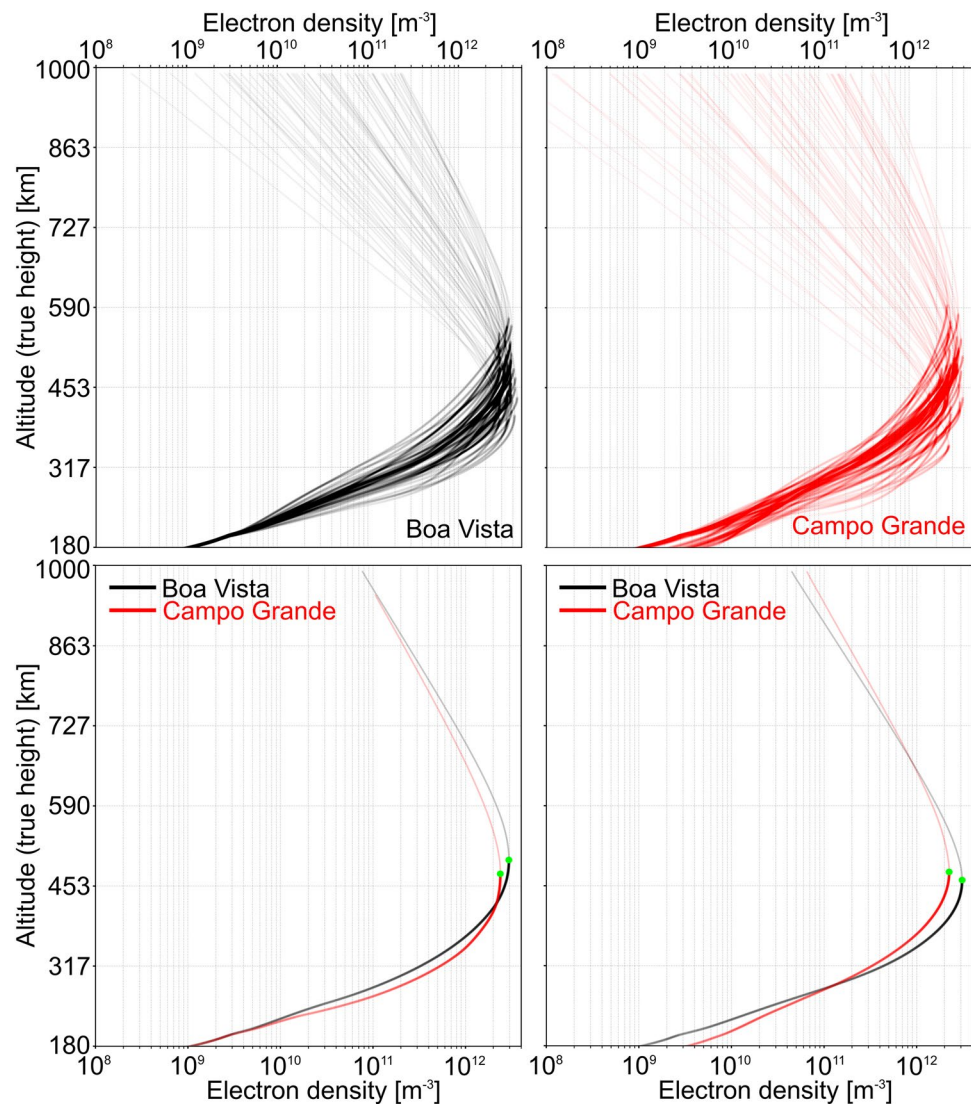
that the southern EIA crest was not reaching the latitude of the station previously. The opposite trend is verified over station BV, initially with larger values of TEC that suddenly decrease during its pre-reversal time, possibly suggesting that the EIA northern crest located over the station was moved northward. Notwithstanding, tens of minutes after the PRE, when the EPB events were verified in the dataset, the ambient vertical drift component is known to decrease steeply, sometimes reaching negative values. Hence, the initial spatial distribution of the EIA (crest over BV) is likely to be restored after the Vz_p, when the scintillation is typically registered, potentially causing asymmetries in the S₄ magnitude due to the distinct ionospheric background.

The upper panels of Fig. 9 present the N_e profiles gathered during the COPEX campaign (55 days) for BV (left) and CG (right) for the same time interval considered in Fig. 8. The results indicate that the overall N_e peak seems to be slightly larger for BV; meanwhile, the hmF2 is lower. Moreover, the

bottomside distribution over BV is less scattered (more condensed) than over CG, especially for lower altitudes. These profiles of the entire campaign suggest that the F layer thickness over CG is typically broader than over BV; ergo, L^{-1} is more pronounced over station BV.

The lower left/right panels show the average of the N_e profiles for BV (black) and CG (red) along the months of October/November–December. The months were separated to elucidate that the seasonal variation of the Vz_p along the transition from equinox to the summer solstice is directly related to the background differences between the hemispheres, which in turn are believed to cause the asymmetries in the scintillation scenario. For information, the equatorial Vz_p average values were 47.6 m/s, 55.1 m/s, and 60.7 m/s for October, November and December, respectively. The green dots correspond to the hmF2 in each case. As can be easily noticed, the CG profile always initiates from a lower altitude and eventually reaches/surpasses the BV profile

Fig. 9 Electron density (N_e) profiles obtained during COPEX campaign. Upper panels: mass plot of the N_e profiles during COPEX for the stations of BV (left) and CG (right). Lower panel: N_e average profiles during October (left) and November–December (right). The green dots correspond to the N_e peak altitudes



altitudes, again revealing the persistent (increasing) trend of a thicker profile (i.e., smaller L^{-1}) synchronously with the Vzp enhancement. The average N_e peak is consistently larger over BV, although a transition in hmF2 occurred from equinox up to summer solstice season, with the hmF2 over CG eventually becoming higher. These features are in conformity with the discussion of Fig. 8 and indicate that these aspects are coherent along the months evaluated.

The upper panel of Fig. 10 shows the differences between the altitudes of the N_e profiles [$\Delta h = h(\text{BV}) - h(\text{CG})$] for the same time interval evaluated in Figs. 8 and 9 for the entire COPEX campaign. Δh was calculated up to the hmF2 altitudes. The colors from blue to red were used as a visual tool to represent the seasonal transition from October to

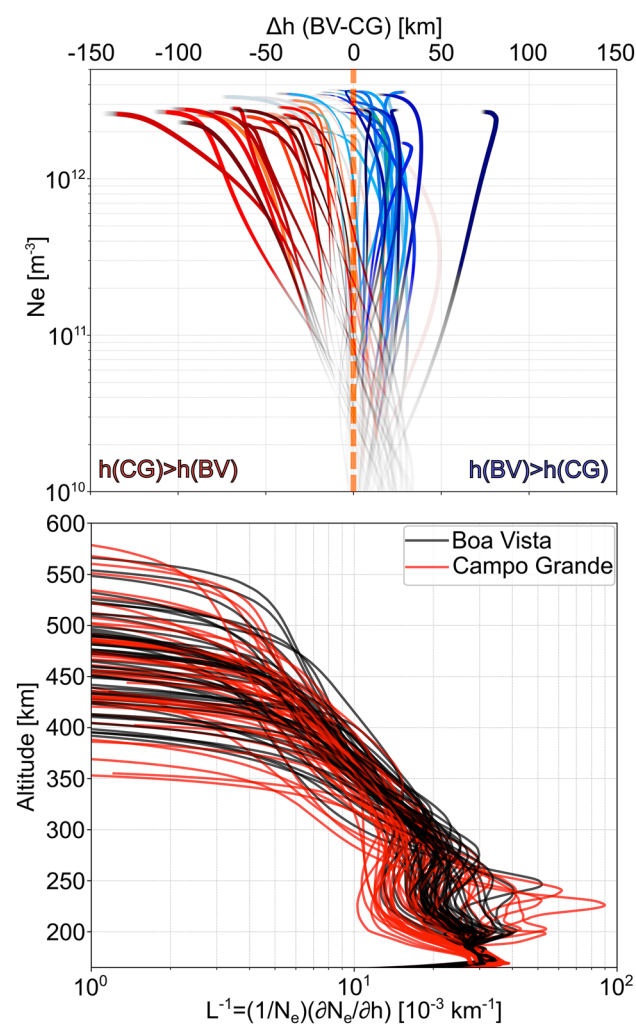


Fig. 10 Comparison between ionospheric electron density altitudes and bottomside vertical gradient scale length over the conjugate stations. Upper panel: differences between the altitudes of the N_e profiles over BV and CG during the COPEX campaign. The colors were used as a visual tool to illustrate the seasonal trend, with blue/red corresponding to October/December. Lower panel: N_e bottomside gradient scale length for BV (black) and CG (red)

December. Positive/negative values of Δh correspond to higher altitudes over BV/CG. The red dashed line stands for the equivalence level ($\Delta h = 0$). Please notice that for the entire period, the smaller values of N_e (i.e., the bottomside) correspond to positive Δh ; therefore, $h(\text{BV})$ is predominantly higher than $h(\text{CG})$ at lower altitudes. This result may be directly associated with the onset time difference between stations. According to the rise of the equatorial EPB structures, they will reach conjugate points along the geomagnetic field lines from below up to a given altitude, depending on the equatorial apex. Hence, being $h(\text{CG})$ at the bottomside consistently lower, it must be often reached earlier as well.

For some cases during October $h(\text{BV}) > h(\text{CG})$ up to the N_e peak, but please notice that according to the transition to November and December (i.e., from blue to red), $h(\text{CG})$ increases, becoming substantially higher than $h(\text{BV})$ around the N_e peak, although starting at lower altitudes. This result reinforces the hypothesis of an often larger L^{-1} over station BV; but this will be discussed afterward.

Xiong et al. (2016) and Wan et al. (2018) found tangible results showing that scintillation may take place also up to the topside (about 500 km). These altitudes are around the hmF2 region in the lower panels of Fig. 9; thus, let the Δh to be considered over the entire N_e profile in the upper panel of Fig. 10 (i.e., from bottomside up to hmF2). In this case, the vast majority of the variation resides $-140 \text{ km} \leq \Delta h \leq 40 \text{ km}$. Typical EPB rise velocities (V_{EPB}) obtained through spaced ionosonde observations over the Brazilian territory presented in Abdu et al. (1983) suggest a range of $30 \text{ m/s} \leq V_{\text{EPB}} \leq 300 \text{ m/s}$. Thus, let also the average to be considered, i.e., $V_{\text{EPB}} = 165 \text{ m/s}$, therefore, the differences between the altitudes, $-140 \text{ km} \leq \Delta h \leq 40 \text{ km}$, imply (in absolute values) an onset difference around $0.24 \text{ h} \leq \Delta t \leq 0.07 \text{ h}$. This value is very close to the mean (μ) S_4 onset difference between the conjugate stations demonstrated to be around 0.21 h (about 12 min).

The lower panel of Fig. 10 exhibits the bottomside N_e gradient scale length for BV (black) and CG (red). It is clear that L^{-1} is predominantly larger over BV, except for a few cases during October. Paznukhov et al. (2012) found that the depth of TEC depletions are directly correlated with the scintillation intensities. Abdu et al. (2020) showed that cases of larger bottomside N_e gradient (L^{-1}) also resulted in stronger levels of depletion. The results presented in the lower panel of Fig. 10 comply with their findings. Please notice that when the EPBs reach stations BV and CG, these structures will undergo distinct values of thickness, vertical gradients in N_e , and TEC. Over BV the combination of the EPB depletion, larger N_e peak and the larger L^{-1} results in an enhancement in the abruptness of the spatial plasma density gradient along the signal path. This can be one of the possible explanations for the asymmetry in the S_4 intensity. The

similar trend of the seasonal increase in L^{-1} asymmetry, in Δh , and V_{zp} , seems to support the hypothesis that the vertical drift component controls such scintillation asymmetries.

Additionally, one must notice that the distinct vertical drift pattern over each hemisphere causes an asymmetry in the fountain effect; hence, the EIA crests in the southern/northern hemisphere may be located farther/closer to the CG/BV stations during the EPBs, also contributing to the differences in the N_e peak. As a result, the neighborhood of station BV typically contains a larger portion of the EIA crest when compared to station CG, as is already suggested by the lower right panel in Fig. 8 and lower panels in Fig. 9. Khadka et al. (2018) also verified that during the months of October–February, the EIA crest is usually closer to the equator in the northern hemisphere (e.g., Fig. 2 in their paper). However, it must be mentioned that their results are for the Peruvian region. Hence, the asymmetric EIA distribution over BV and CG may also contribute to the abruptness of the plasma density spatial gradient along the signal path in the northern hemisphere, possibly having implications for the larger S_4 over station BV.

Please notice that although the maximum values of S_4 typically occurred over BV, when the entire night is considered the scintillation over CG may be more long-lasting, and the “net scintillation bulk” may be larger over CG. Zhao et al. (2021) have recently reported this hemispheric aspect. In fact, Fig. 3 exemplifies a steeper peak over BV; conversely, the S_4 is more persistent over CG, despite being smoother. In addition, the right panel of Fig. 7 shows a broader S_4 curve, although with smaller peak values. This is expected because the smaller N_e thickness over BV (i.e., larger vertical gradient), especially towards summer solstice, carries an intrinsic flaw, viz. a larger chemical loss rate along the night; therefore, the density is likely to be damped faster over BV.

In summary, meridional winds and geomagnetic field features may alter the vertical plasma drift in both the hemispheres. These diverse vertical drift profiles, in turn, will cause distinct background conditions, changing F region altitudes, ionization loss, F region thickness, bottomside electron density gradient scale length, TEC, etc. According to the scintillation data, these ensuing events imply some deviations on the scintillation onset and strength patterns over each hemisphere.

Conclusion

According to the analysis presented, the asymmetry in the vertical plasma drift is believed to be caused by the meridional winds and geomagnetic field spatial configuration, possibly causing distinct profiles of F region

altitudes, ionization loss, F region thickness, bottomside electron density gradient scale length, and TEC over both conjugate stations. This diverse background in each hemisphere seems to cause a certain level of inequality in the amplitude scintillation (S_4) onset and magnitude. Thus, although the stations experience the same EPB event, the ionospheric background plays a substantial role in the subsequent occurrence and intensity of scintillation. The main findings of this work may be summarized as follows:

1. The amplitude scintillation (S_4) onset occurred earlier over station CG (southern hemisphere) in 80% of the cases (44 days), and the geomagnetic activity did not play any substantial role in this trend. The calculated mean value (μ) of this S_4 onset difference (Δt) was about 12 min with a standard deviation (σ) about 22 min. This variability is expected because of the large number of parameters involved in the phenomenology.
2. The trend of later S_4 onset over station BV (northern hemisphere) occurred at all levels of V_{zp} (> 20 m/s), either considering the equatorial V_{zp} value or using the V_{zp} values over each station.
3. The maximum values of S_4 follow a trend opposite to that of Δt , i.e., the scintillation is often (71% of the cases) stronger over station BV (northern hemisphere) when compared to station CG (southern hemisphere). This trend seems to increase toward the summer solstice (in the southern hemisphere), hence reinforcing the hypothesis of the role of the vertical drift asymmetry in this behavior.
4. These S_4 onset and peak asymmetries are persistent across the entire dataset as shown by the right panel of Fig. 7.
5. The lower bottomside over station CG seems to explain the earlier S_4 onset consistently. The differences between the altitudes over the conjugate stations, Δh , suggest EPB velocities compatible to the delays of S_4 onset presented in Fig. 4.
6. Over BV, a steeper L^{-1} , i.e., a smaller F region thickness, and a larger TEC due to the EIA crest may imply an enhancement in the abruptness of spatial gradients along the signal path, possibly causing the higher values of S_4 .

This work shows that the vertical component of the plasma drift may be responsible for controlling important parameters of the ionospheric background, resulting in changes of scintillation onset and magnitude. Future works must evaluate the mechanisms behind the vertical drift variability and other aspects of the conjugated asymmetry of the scintillation in order to improve the current predictive capabilities.

Acknowledgements J. Sousasantos greatly acknowledges FAPESP for support under process 2018/06158-9. M. A. Abdu acknowledges the support received from the São Paulo State Foundation for Promotion of Research (FAPESP) through the Process 2016/24970-7, the support received from the Ministry of Science and Technology and Conselho Nacional de Desenvolvimento Científico e Tecnológico (CNPq) through process 03083/2011-5, and Coordenação de Aperfeiçoamento de Pessoal de Nível Superior (Capes) for a senior visiting professorship at ITA/DCTA. E. R. de Paula acknowledges CNPq grant 202531/2019-0, and INCT GNSS-NavAer Grants 2014/465648/2014-2 (CNPq) and 2017/50115-0 (FAPESP). A. O. Moraes is grateful to CNPq for Awards 309389/2021-6 and 314043/2018-7. L. A. Salles acknowledges CAPES for financial support under process 88887.495093/2020-00. The authors thank all the GIRO and OMNIWeb staffs. Authors also acknowledge A. L. A. Silva for his valuable assistance.

Data availability Digisonde data may be accessed at <https://ulcar.uml.edu/DIDBase/>. Scintillation data may be accessed at https://zenodo.org/record/6514603#_ynMtLNPMD8 and https://zenodo.org/record/6514344#_ynMtLNPMD8. Kp data may be accessed at <https://omniweb.gsfc.nasa.gov>. The OMNI data were obtained from the GSFC/SPDF OMNIWeb interface at <https://omniweb.gsfc.nasa.gov>. All-sky data may be accessed at <https://doi.org/10.5281/zenodo.5939786>.

References

- Abdu MA, de Medeiros RT, Sobral JHA, Bittencourt JA (1983) Spread F plasma bubble vertical rise velocities determined from spaced ionosonde observations. *J Geophys Res* 88(A11):9197–9204. <https://doi.org/10.1029/JA088iA11p09197>
- Abdu MA et al (2009) Conjugate point equatorial experiment (COPEX) campaign in Brazil: electrodynamics highlights on spread F development conditions and day-to-day-variability. *J Geophys Res* 114(A04308):1–21. <https://doi.org/10.1029/2008/JA013749>
- Abdu MA, Kherani EA, Sousasantos J (2020) Role of bottom—side density gradient in the development of equatorial plasma bubble/spread F irregularities: solar minimum and maximum conditions. *J Geophys Res* 125:1–15. <https://doi.org/10.1029/2020JA027773>
- Beach TL, Kintner PM (2001) Development and use of a GPS ionospheric scintillation monitor. *IEEE Trans Geosci Remote Sens* 39(5):918–928. <https://doi.org/10.1109/36.921409>
- Briggs BH, Parkin IA (1963) On the variation of radio star and satellite scintillations with zenith angle. *J Atmos Terr Phys* 25:339–365. [https://doi.org/10.1016/0021-9169\(63\)90150-8](https://doi.org/10.1016/0021-9169(63)90150-8)
- de Paula ER, Muella MTAH, Sobral JHA, Abdu MA, Batista IS, Beach TL, Groves KM (2010) Magnetic conjugate point observations of kilometer and hundred-meter scale irregularities and zonal drifts. *J Geophys Res* 115(A8):1–15. <https://doi.org/10.1029/2010JA015383>
- Dungey JW (1956) Convective diffusion in the equatorial F region. *J Atmos Terr Phys* 9(5):304–310. [https://doi.org/10.1016/0021-9169\(56\)90148-9](https://doi.org/10.1016/0021-9169(56)90148-9)
- Fejer BG, Scherliess L, de Paula ER (1999) Effects of the vertical drift velocity on the generation and evolution of spread F. *J Geophys Res* 104(A9):19859–19869. <https://doi.org/10.1029/1999JA900271>
- Haerendel G (1973) Theory of equatorial spread F. Preprint, Max-Planck-Institut für extraterrestrische Physik, Garching bei München, Germany
- Huang CS (2018) Effects of the postsunset vertical plasma drift on the generation of equatorial spread F. *Prog Earth Planet Sci* 5(3):1–15. <https://doi.org/10.1186/s40645-017-0155-4>
- Khadka SM, Valladares CE, Sheehan R, Gerrard AJ (2018) Effects of electric field and neutral wind on the asymmetry of equatorial ionization anomaly. *Radio Sci* 53:683–697. <https://doi.org/10.1029/2017RS006428>
- Kintner PM, Ledvina BM, de Paula ER (2007) GPS and ionospheric scintillations. *Space Weather* 5(S09003):1–23. <https://doi.org/10.1029/2006SW000260>
- Luo X, Xiong C, Gu S, Lou Y, Stolle C, Wan X, Liu K, Song W (2019) Geomagnetically conjugate observations of equatorial plasma irregularities from Swarm constellation and ground-based GPS stations. *J Geophys Res* 124(5):3650–3665. <https://doi.org/10.1029/2019JA026515>
- Moraes AO, Vani BC, Costa E, Abdu MA, de Paula ER, Sousasantos J, Monico JFG, Forte B, Negreti PMS, Shimabukuro MH (2018a) GPS availability and positioning issues when the signal paths are aligned with ionospheric plasma bubbles. *GPS Solut* 22(95):1–12. <https://doi.org/10.1007/s10291-018-0760-8>
- Moraes AO, Muella MTAH, de Paula ER, de Oliveira CBA, Terra WP, Perrella WJ, Meibach-Rosa PR (2018b) Statistical evaluation of GLONASS amplitude scintillation over low latitudes in the Brazilian territory. *Adv Space Res* 61(7):1776–1789. <https://doi.org/10.1016/j.asr.2017.09.032>
- Moraes AO, Vani BC, Costa E, Sousasantos J, Abdu MA, Rodrigues F, Gladek YC, de Oliveira CBA, Monico JFG (2018c) Ionospheric scintillation fading coefficients for the GPS L1, L2, and L5 frequencies. *Radio Sci* 53(9):1165–1174. <https://doi.org/10.1029/2018RS006653>
- Ossakow SL (1981) Spread-F theories—a review. *J Atmos Terr Phys* 43(5–6):437–452. [https://doi.org/10.1016/0021-9169\(81\)90107-0](https://doi.org/10.1016/0021-9169(81)90107-0)
- Paznukhov VV et al (2012) Equatorial plasma bubbles and L-band scintillations in Africa during solar minimum. *Ann Geophys* 30:675–682. <https://doi.org/10.5194/angeo-30-675-2012>
- Resende LCA, Denardini CM, Picanço GAS, Moro J, Barros D, Figueiredo CAOB, Silva RP (2019) On developing a new ionospheric plasma index for Brazilian equatorial F region irregularities. *Ann Geophys* 37:807–818. <https://doi.org/10.5194/angeo-37-807-2019>
- Sobral JHA et al (2009) Ionospheric zonal velocities at conjugate points over Brazil during the COPEX campaign: experimental observations and theoretical validations. *J Geophys Res* 114(A04309):1–24. <https://doi.org/10.1029/2008JA013896>
- Sousasantos J, Kherani EA, Sobral JHA (2013) A numerical simulation study of the collisional-interchange instability seeded by the pre-reversal vertical drift. *J Geophys Res* 118(11):7438–7449. <https://doi.org/10.1002/2013JA018803>
- Sousasantos J, Moraes AO, Sobral JHA, Muella MTAH, de Paula ER, Paolini RS (2018) Climatology of the scintillation onset over Southern Brazil. *Ann Geophys* 36:565–576. <https://doi.org/10.5194/angeo-36-565-2018>
- Sousasantos J, Kherani EA, Sobral JHA, Abdu MA, Moraes AO, Abud CBA (2019) A numerical study on the 3-D approach of the equatorial plasma bubble seeded by the pre-reversal vertical drift. *J Geophys Res* 124(6):4539–4555. <https://doi.org/10.1029/2018JG026239>
- Sousasantos J, Abdu MA, Santos AM, Batista IS, Silva ALA, Loures da Costa LEV (2020) Further complexities on the pre-reversal vertical drift modeling over the Brazilian region: a comparison between long-term observations and model results. *J Space Weather Space Clim* 10(20):1–9. <https://doi.org/10.1051/swsc/2020022>
- Wan X, Xiong C, Rodriguez-Zuluaga J, Kervalishvili GN, Stolle C, Wang H (2018) Climatology of the occurrence rate and amplitudes of local time distinguished equatorial plasma depletions observed by Swarm satellite. *J Geophys Res* 123(4):3014–3026. <https://doi.org/10.1002/2017JA025072>

- Whitney HE, Basu S (1977) The effect of ionospheric scintillation on VHF/UHF satellite communications. *Radio Sci* 12(1):123–133. <https://doi.org/10.1029/RS012i001p00123>
- Xiong C, Stolle C, Lühr H (2016) The Swarm satellite loss of GPS signal and its relation to ionospheric plasma irregularities. *Space Weather* 14(8):563–577. <https://doi.org/10.1002/2016SW001439>
- Yeh KC, Liu C-H (1982) Radio wave scintillations in the ionosphere. *Proc IEEE* 70(4):324–360. <https://doi.org/10.1109/PROC.1982.12313>
- Zhao X, Xie H, Hu L, Sun W, Hao X, Ning B, Takahashi H, Li G (2021) Climatology of equatorial and low-latitude F region kilometer-scale irregularities over the meridian circle around 120°E/60°W. *GPS Solutions* 25(20):1–14. <https://doi.org/10.1007/s10291-020-01054-2>

Publisher's Note Springer Nature remains neutral with regard to jurisdictional claims in published maps and institutional affiliations.

J. Sousasantos graduated in Mathematics at the Universidade de Taubaté, Brazil, in 2010. M. Sc. (2013) and Dr. Sc. (2017) degrees obtained at the Instituto Nacional de Pesquisas Espaciais. He is currently a Postdoctoral Associate at Instituto Tecnológico de Aeronáutica. His main area of interest is mathematical modeling and forecasting of ionospheric irregularities and atmospheric-ionospheric vertical coupling.

M. A. Abdu received a Ph.D. degree in 1967 from Gujarat University, India. He has been a postdoctoral research fellow at the University of Western Ontario (1968–1971), a professor at CRAAM Mackenzie

University, Sao Paulo (1971–1973), a research scientist since 1973 at the Instituto Nacional de Pesquisas Espaciais, and presently a visiting professor at ITA. His research interests are in space weather and ionospheric physics.

E. R. de Paula obtained a M. Sc. degree at Telecommunications at ITA, and a Dr. Sc. in Geophysics at Instituto Nacional de Pesquisas Espaciais, where he has been working as a researcher for 40 years. He attended postdoc programs at the Utah State University, Logan, for 5 years. His main area of interest is ionospheric physics, focusing on ionospheric scintillations detected by radars and GPS receivers.

A. O. Moraes received the B.S. in telecommunications engineering from Universidade de Taubaté, Brazil, in 2003 and a Dr. Sc. at the Instituto Tecnológico de Aeronáutica, Brazil, in 2013 and has been an engineer at the Instituto de Aeronáutica e Espaço since 2004 and graduate professor since 2015.

L. A. Salles received the B.S. in Electrical Engineering from Universidade de Taubaté, Brazil in 2010, and M. Sc. at the school of Space Sciences and Technologies at Instituto Tecnológico de Aeronáutica, Brazil in 2020. Currently, he is a Ph.D. candidate.

B. J. Affonso received the B.S. in Electrical Engineering (2012) from Universidade Estadual Paulista Júlio de Mesquita Filho and M.Sc. in Aeronautical Engineering (2016) at the Instituto Tecnológico de Aeronáutica. He is currently a PhD candidate at the Instituto Tecnológico de Aeronáutica (ITA) working with the effects of the ionosphere on the GPS signal and since 2014 has been working as Avionics System Engineer at Embraer, focusing on navigation systems.